Shock excited far-infrared molecular emission around T Tau[*]

L. Spinoglio[1], T. Giannini[1,2,3], B. Nisini[2], M.E. van den Ancker[4], E. Caux[5], A.M. Di Giorgio[1], D. Lorenzetti[2], F. Palla[6], S. Pezzuto[1], P. Saraceno[1], H.A. Smith[7], and G.J. White[8,9]

[1] Istituto di Fisica dello Spazio Interplanetario, CNR, via Fosso del Cavaliere 100, 00133 Roma, Italy
[2] Osservatorio Astronomico di Roma, via Frascati 33, 00040 Monte Porzio, Italy
[3] Istituto Astronomico, Università La Sapienza, via Lancisi 29, 00161 Roma, Italy
[4] Astronomical Institute "Anton Pannekoek", University of Amsterdam, Kruislaan 403, 1098 SJ Amsterdam, The Netherlands
[5] CESR, B.P. 4346, 31028 Toulouse Cedex 04, France
[6] Osservatorio Astrofisico di Arcetri, Largo E. Fermi 5, 50125 Firenze, Italy
[7] Harvard – Smithsonian Center for Astrophysics, 60 Garden Street, Cambridge, MA, USA
[8] Physics Department, Queen Mary & Westfield College, University of London, Mile End Road, London E1 4NS, UK
[9] Stockholm Observatory, 133 36 Saltsjobaden, Sweden

Abstract. The first complete far-infrared spectrum of T Tau has been obtained with the LWS spectrometer on-board the Infrared Space Observatory (ISO), which detected strong emission from high-J (J=14-25) CO, para- and ortho-H_2O and OH transitions over the wavelength range from 40 to 190 μm. In addition the [OI]63μm, [OI]145μm and [CII]158μm atomic lines were also detected. Most of the observed molecular emission can be explained by a single emission region at T$\sim$300-900 K and n_{H_2} $\sim 10^{5-6} cm^{-3}$, with a diameter of about 2-3 arcsec. This corresponds to a very compact region of 300 - 400 AU at the distance of 140 pc. A higher temperature component seems to be needed to explain the highest excitation CO and H_2O lines. We derive a water abundance of 1-7 $\cdot 10^{-5}$ and an OH abundance of $\sim 3 \cdot 10^{-5}$ with respect to molecular hydrogen, implying H_2O and OH enhancements by more than a factor of 10 with respect to the expected ambient gas abundance.

The observed cooling in the various species amounts to 0.04 $L_\odot$, comparable to the mechanical luminosity of the outflow, indicating that the stellar winds could be responsible of the line excitation through shocks.

In order to explain the observed molecular cooling in T Tau in terms of C-type shock models, we hypothesise that the strong far-ultraviolet radiation field photodissociates water in favour of OH. This would explain the large overabundance of OH observed.

The estimated relatively high density and compactness of the observed emission suggest that it originates from the shocks taking place at the base of the molecular outflow emission, in the region where the action of the stellar winds from the two stars of the binary system is important.

1. Introduction

T Tau has been extensively studied from radio to ultraviolet wavelengths because it has long been considered the prototype of a class of pre-main sequence stars. In recent years it has become clear that T Tau is in reality a very complex system and that it differs from other T Tauri stars. It is in fact known to be a binary system (Dyck et al. 1982), containing an optical stellar component (T Tau N) and an infrared companion 0.7 arcsec to the south (T Tau S), corresponding to 100 AU at the 140 pc distance of the Taurus Auriga dark cloud (Wichmann et al. 1998). T Tau S dominates the bolometric luminosity of the system (Ghez et al. 1991), but it has no detectable optical counterpart to a limiting magnitude of V=19.6, suggesting an optical extinction greater than 7 mag (Stapelfeldt et al. 1998).

Since Herbig's (1950) optical spectra of Burnham's nebula, surrounding T Tau several arcsecond across, resembling a so-called HH object, it was clear that the interaction of stellar winds with the surrounding molecular medium is at work. Molecular outflow activity was first mapped by Edwards & Snell (1982) in ^{12}CO J=1-0 and J=2-1, who found that 95% of the high velocity molecular gas is associated with blueshifted material. The direction of the detected outflow is roughly parallel to the line of sight, but the emission also shows a region extending 2 arcmin to the south and east of T Tau N with a secondary peak in the blueshifted wing. Higher resolution maps of the ^{12}CO J=3-2, J=6-5 and $C^{18}O$ J=1-0, J=2-1 and HCO+ emission later showed (Schuster et al. 1993, Momose et al. 1996, Schuster et al. 1997, Hogerheijde et al. 1998) a complex outflow system that could originate from the different components of the binary system.

The fast stellar winds observed through forbidden optical line emission (Böhm & Solf 1994), revealed five distinct kinematic components that suggest that both the primary star and the companion may drive separate bipolar outflows. A giant Herbig-Haro flow was recently discovered (Reipurth et al. 1997) around T Tau and is interpreted as originating several thousand years ago from T Tau S.

Strong and extended H_2 ro-vibrational emission was found quite early around T Tau (Beckwith et al. 1978). Recently, high resolution H_2 imaging (Herbst et al. 1996, 1997) indicated that the extended molecular hydrogen emission arises from the impact on the ambient cloud of two outflow systems oriented NW-SE and E-W. These originate from the two stars, each with its circumstellar disk, and the emission is distributed equally over T Tau N and T Tau S. Infrared adaptive optics observations in H_2 show instead that the emission is concentrated on T Tau S and is interpreted in terms of shocks occurring as matter accretes onto the circumstellar disk of T Tau S (Quirrenbach & Zinnecker 1997). No firm conclusion is therefore reached on this problem.

T Tau has associated a substantial amount of mass of dust, it is therefore luminous in the millimeter continuum (Adams et al. 1990, Beckwith et al. 1990). A circumstellar disk has been detected both with CO interferometry and infrared scattered light (Weintraub et al. 1989, Momose et al. 1996). Later, millimeter continuum interferometry at 0.9 and 3mm (Hogerheijde et al. 1997, Akeson et al. 1998, respectively) was used to derive a total mass of 0.04 $M_\odot$ for the circumstellar disk around T Tau N and at least 10 times smaller for that associated to T Tau S. A circumbinary envelope would also be required to fit the continuum energy distribution.

Far-infrared spectroscopy provides powerful diagnostic lines from abundant molecular species like CO, H_2O and OH, that can be used to clarify the physical processes at work in the complex T Tau system. In this paper we present the far-infrared spectrum observed from the Long Wavelength Spectrometer (LWS, Clegg et al. 1996) onboard the Infrared Space Observatory (ISO, Kessler et al. 1996). Additional data from the Short Wavelength Spectrometer (SWS, de Graauw et al. 1996) are also used for discussing the molecular emission properties. The main results of the SWS are presented by van den Ancker et al. (1999). The continuum far-infrared spectrum of T Tau will be discussed in a forthcoming paper (Pezzuto et al. in preparation).

2. Observations

T Tau has been observed with ISO (Infrared Space Observatory) using the LWS (Long Wavelength Spectrometer, Clegg et al. 1996). A full low resolution (R $\sim$ 200) spectrum of the source from 45 to 197 μm was obtained during revolution 680, corresponding to September 25, 1997. The beamsize is on average 80 arcsec, depending on the wavelength. The spectrum was made up of 23 full grating scans oversampled at 1/4 of a resolution element, with each spectral sample integrated for 11.5 sec, with a total integration time of 4052 sec. Besides the observation on-source, full grating spectra were also collected
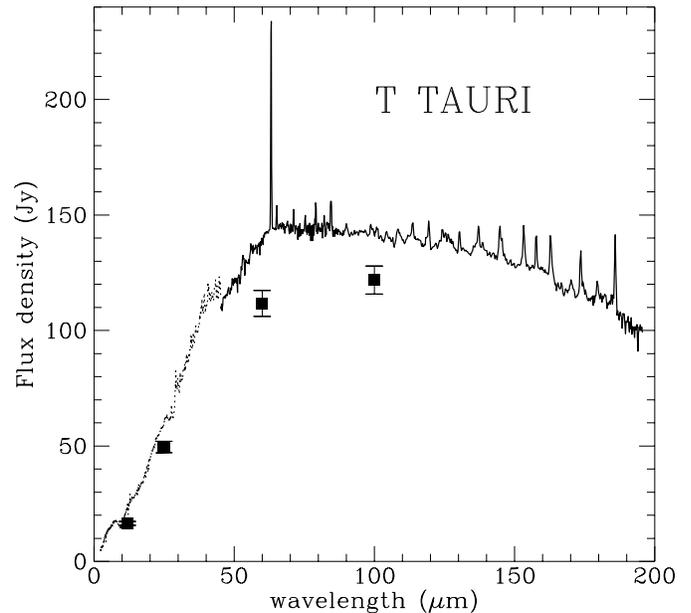
Fig. 1. The complete ISO LWS and SWS spectrum of T Tau. The IRAS data are also shown for comparison.

Table 1. Journal of the ISO-LWS observations of T Tau.

| Pos.	2000.0 Coordinates R.A. DEC.	OTT
	h m s deg ' "	(sec)
T Tau on	4:21:59.4 +19:32:06.5	4265
T Tau off N	4:21:59.4 +19:33:46.5	1345
T Tau off S	4:21:59.3 +19:30:26.5	1345
T Tau off W	4:22:06.4 +19:32:06.0	1345
T Tau off E	4:21:52.4 +19:32:07.0	1345

at four off-source positions. In Table 1 we present the journal of the LWS observations, which includes source and off-source positions and total observing time (OTT), including overheads.

The raw data were reduced and calibrated using version 7 of the LWS pipeline, which achieves an absolute accuracy of about 30% (Swinyard et al. 1998). Post-pipeline processing was carried out with the ISAP package and included removal of spurious signals due to cosmic ray impacts and averaging the grating scans of each detector.

Besides the data measured by the LWS, we also discuss in this paper the detection of H_2O and OH emission lines observed by the SWS. The details of these observations are reported by van den Ancker et al.(1999).

3. Results

The 2-200 μm far-infrared spectrum of T Tau composed by the ISO LWS and SWS spectra is shown in Fig. 1. The displacement (of $\sim$ 15%) between the flux level of the two instruments at $\sim$ 45μm is well within the calibration uncertainties. In the figure, IRAS photometry is also reported for comparison. As discussed in van den Ancker et al. (1999), the higher ISO fluxes
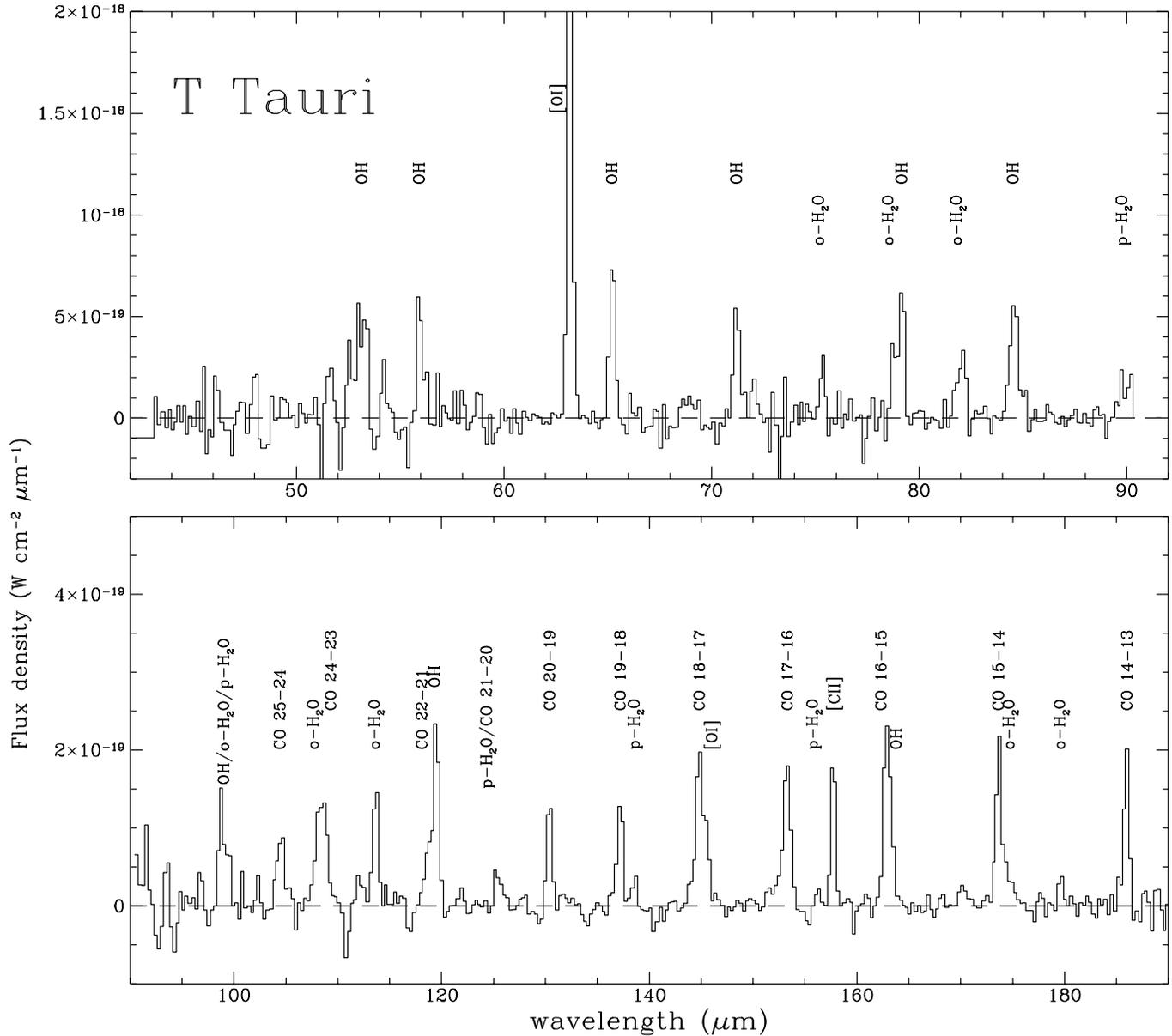
Fig. 2. The ISO-LWS emission line spectrum of T Tau, from which the continuum has been subtracted.

compared to the IRAS data (30-50%) can be explained by the flare that occurred to the system in 1990-1991 (Ghez et al. 1991; Kobayashi et al. 1994), after which the infrared luminosity of T Tau did not return to the pre-outburst value.

The line spectrum (Fig. 2) is very rich in molecular emission lines from the rotational spectra of carbon monoxide, water and hydroxyl. The line fluxes, computed by fitting gaussian profiles to the lines, are listed in Tables 2-5. All of the CO transitions with $J_{up} = 14$-25 appear in the spectrum. However, we cannot assign a flux, but only an upper limit, to the $J_{up} = 23$ line because it is blended with the water line o-H_2O 4_{14}-3_{03}. Water lines are observed both in the ortho (o-) and para (p-) form. Most of the back-bone lines up to excitation temperatures of more than 700 K are detected for ortho-H_2O and up to nearly 400 K for the para-H_2O, as well as most of the strongest transitions falling

in the LWS spectral range. Also the strong OH lines are detected and are particularly strong, with excitation temperatures up to 600 K. [OI]63μm and 145μm and [CII]158μm are the only atomic lines present in the ISO-LWS spectrum. [OI]63μm emission from T Tau was already detected with the Kuiper Airborne Observatory from Cohen et al. (1988), who measured a total flux in a 47$''$ aperture of $(242 \pm 25) \times 10^{-20}$ W cm^{-2}, which is consistent with our value, which is however much more precise. This indicates that the flare occurred in 1990-91 did not influence the far-infrared line emission. In the four off-source positions only the [CII]158μm line was detected (see Sect. 3.4 and Table 5).

A large velocity gradient (LVG) code, solving the level population equations in a plane parallel geometry (Nisini et al. 1999a, Giannini et al. 1999) was used to model the observed

Table 2. Measured CO line fluxes from the LWS grating spectrum, with 1σ uncertainties. Upper limits are at 3σ.

λ_{obs} (μm)	Line id.	λ_{vac} (μm)	F (10^{-20} W cm^{-2})	ΔF
	CO 28-27	93.35	<4.1	
	CO 27-26	96.77	<5.3	
	CO 26-25	100.46	<5.3	
104.40	CO 25-24	104.44	7.0	1.3
108.81	CO 24-23	108.76	6.7	1.1
	CO 23-22	113.46	<10.5*	
118.58[†]	CO 22-21	118.58	5.1	0.8
124.31	CO 21-20	124.19	5.2	0.9
130.40	CO 20-19	130.37	7.7	0.5
137.17	CO 19-18	137.20	9.6	0.7
144.78[†]	CO 18-17	144.78	12.6	0.5
153.24	CO 17-16	153.27	14.1	0.4
162.81[†]	CO 16-15	162.81	14.0	0.7
173.63[†]	CO 15-14	173.63	15.5	1.0
185.93	CO 14-13	186.00	14.3	1.0

[†] wavelength was fixed for deblending.

* this line is blended with the o-H_2O 4_{14}-3_{03} (see text), the total flux has a 1σ uncertainty of $0.5 \cdot 10^{-20}$ W cm^{-2}.

Fig. 3. Model fits through the observed CO lines. The range of temperatures and densities compatible with the observations are indicated. The higher observed J lines (J=24, 25 and 26) have fluxes too high to be fitted by the same parameters as the other lines, suggesting the presence of a second component.
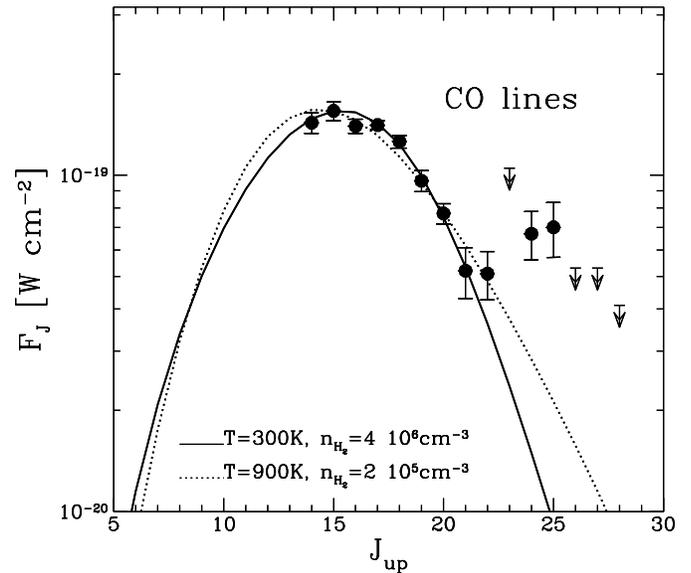
molecular emission line intensities from CO, H_2O and OH. As a first approximation, the local radiation field was not taken into account in the radiation transfer calculations. We will however discuss in Sect. 3.3 what is the effect of considering the infrared local radiation field in the OH model.

The model has many free-parameters (gas temperature and density, intrinsic width of the line, column density and emitting area or filling factor, which is related to both number and column densities) that cannot be easily constrained simultaneously. Given the assumption that all of the molecular lines originate from the same emitting gas, we started our analysis by deriving a range of temperature and density that is allowed from fitting the CO lines, that are likely optically thin. These parameters are then used to model the water and OH lines, which, unlike the CO lines, have high optical depths due to their strong radiative transitions in the far-infrared.

3.1. CO emission

For the CO model, we computed the collisional downward rates for levels with $J_{up} < 60$ and T > 100 K using the γ_{J0} coefficients taken from McKee et al. (1982), while the upward rates were computed using the principle of detailed balance. Radiative decay rates were taken from Chackerian & Tipping (1983).

The distribution of the observed CO line fluxes as a function of the rotational quantum number is shown in Fig. 3. Because the CO lines are optically thin, their emission, in the LVG model considered, does not depend on the velocity gradient and thus on the assumed line-width. We have considered for our fit only the transitions with J_{up} less than 22. Our data are consistent with gas temperatures ranging from T = 300 to 900 K and molecular hydrogen densities of n = 10^{5-6}cm^{-3}. The two extreme models consistent with the data have:

$$T = 300 \text{ K and } n_{H_2} = 4 \cdot 10^6 \text{cm}^{-3};$$
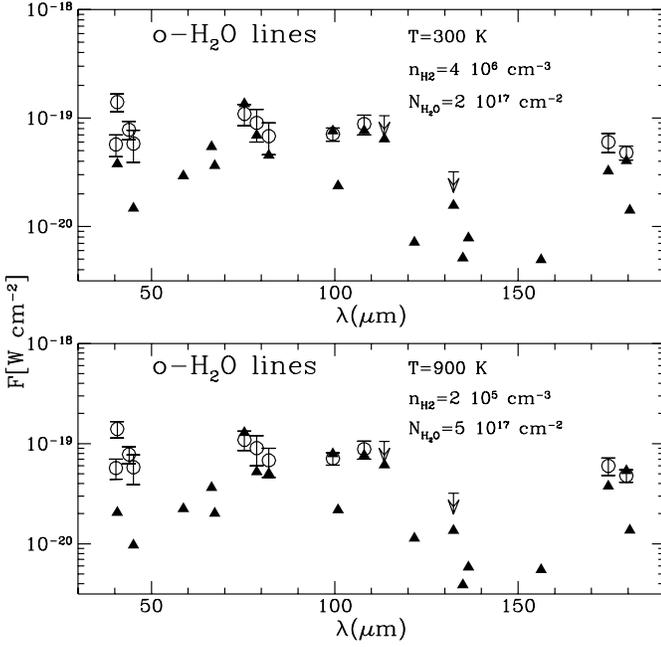$$T = 900 \text{ K and } n_{H_2} = 2 \cdot 10^5 \text{cm}^{-3}.$$

Fig. 3 shows that the transitions with J_{up} = 24 and 25 have a flux level which is too high to be explained by the same gas component of the other lines and may indicate the presence of a warmer gas emission. This warmer component, which cannot easily be constrained by the higher J_{up} transitions observed, could also affect the J_{up} = 21 and 22 lines. However fitting the component covering the lines $14 \leq J_{up} \leq 20$, results in the same parameters as the low temperature model above.
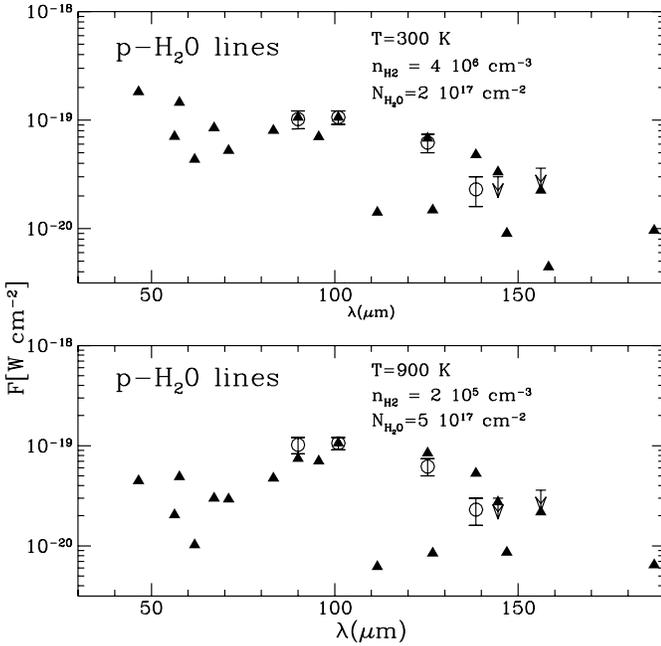
3.2. H_2O emission

As outlined in the previous section we adopted the temperature and density as derived from the CO lines models to fit the observed H_2O line fluxes.

We considered in the computation 45 levels for both the ortho and para species (*i.e.* excitation energies up to $\sim$ 2000 K): radiative rates are taken from Chandra et al. (1984) while the H_2O-H_2 collision rates are derived from Green et al. (1993). We assumed an ortho/para abundance ratio of 3, equal to the ratio of the statistical weigths of their nuclear spins.

The other parameters that enter in the model are the velocity gradient in the region (dV/dr) and the projected area of the emission region. The optical depth in the lines is directly proportional to the water column density (N(H_2O)). Since the ratios of different lines depend on their relative optical depths, we can use them to constrain dV/N(H_2O). On the other hand, the absolute line intensity depends on both the column density and the projected area of the emission region, and therefore if

Fig. 4. Comparison of the modeled ortho-H_2O line fluxes (filled triangles) with those observed (open circles) for the two models considered.

Fig. 5. Comparison of the modeled para-H_2O line fluxes (filled triangles) with those observed (open circles) for the two models considered.

Table 3. Measured water line fluxes from the SWS (upper list) and LWS (lower list) grating spectrum, with 1σ uncertainties. Upper limits are at 3σ.

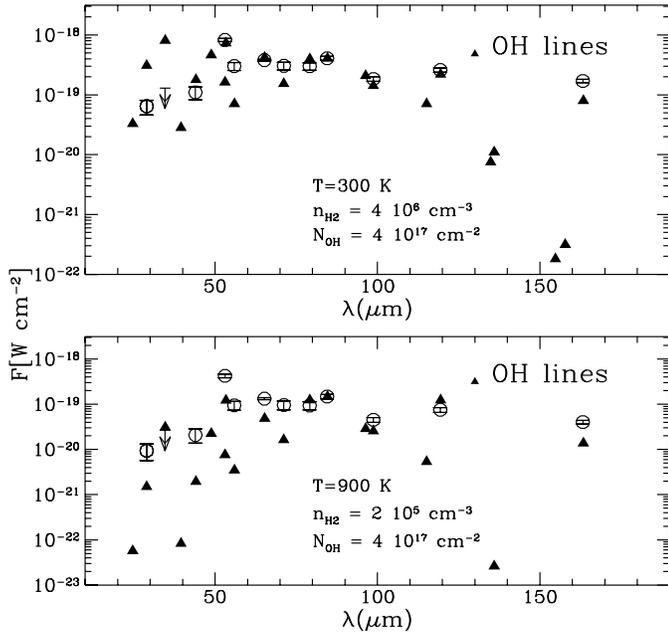| λ_{obs} (μm)	Line id.	λ_{vac} (μm)	F	ΔF
			(10^{-20} W cm^{-2})	
25.940	o-H_2O 5_{41}-4_{14}	25.940	2.4	0.6
29.838	o-H_2O 7_{25}-6_{16}	29.836	4.9	1.1
	o-H_2O 4_{41}-3_{12}	31.771	<3.0	
40.342	o-H_2O 6_{43}-5_{32}	40.337	5.7	1.3
40.688	o-H_2O 4_{32}-3_{03}	40.688	14.1	2.6
43.894[†]	o-H_2O 5_{41}-4_{32}	43.894	7.8	1.5
45.116	o-H_2O 5_{23}-4_{14}	45.111	5.8	1.9
75.35	o-H_2O 3_{21}-2_{12}	75.38	10.9	2.4
78.74[†]	o-H_2O 4_{23}-3_{12}	78.74	9.0	3.0
82.03[†]	o-H_2O 6_{16}-5_{05}	82.03	6.8	2.2
90.05	p-H_2O 3_{22}-2_{11}	89.99	10.2	1.9
99.46[†]	o-H_2O 5_{05}-4_{14}	99.49	7.1	1.0
100.92	o-H_2O 5_{14}-4_{23}	100.91	10.6	1.5
	p-H_2O 2_{20}-1_{11}	100.98		
108.11	o-H_2O 2_{21}-1_{10}	108.07	8.8	1.8
113.65	o-H_2O 4_{14}-3_{03}	113.54	10.5*	
125.39	p-H_2O 4_{04}-3_{13}	125.35	6.2	1.2
	o-H_2O 4_{23}-4_{14}	132.41	<3.2	
138.62	p-H_2O 3_{13}-2_{02}	138.53	2.3	0.7
	p-H_2O 4_{13}-3_{22}	144.52	<3.0	
	p-H_2O 3_{22}-3_{13}	156.19	<3.6	
174.62[†]	o-H_2O 3_{03}-2_{12}	174.63	6.0	1.2
179.58	o-H_2O 2_{12}-1_{01}	179.53	4.8	0.7

[†] wavelength was fixed for deblending.
* this line is blended with the CO 23-22 line (see text), the total flux has a 1σ uncertainty of $0.5 \cdot 10^{-20}$ W cm^{-2}.

the range. On the other hand, we note that the ortho-H_2O lines shortward of 50μm are not fitted by our models. These lines, originated by levels at energies higher than 500 K, are brighter than our predictions, indicating that a warmer component might be required, as also suggested from the higher J CO lines.

An estimate of the intrinsic linewidth dV can be given if we relate the observed emission with the outflow/wind activity taking place in the close environment of the T Tau binary system. The molecular outflow has been traced by different lines at near infrared and millimeter wavelengths (H_2, CO, HCO$^+$), showing linewidths of a few km s^{-1}. Adopting a velocity of 10 km s^{-1}, close to the outflow velocities of 7.9 km s^{-1}(red lobe) and 9.7 km s^{-1}(blue lobe) measured by Levrault (1988) and those measured by Hogerheijde et al. (1998) in ^{13}CO 3-2 (of 12 and 15.6 km s^{-1}for the red and blue lobes, respectively), we derive a water column density of $(2-5)10^{17}$ cm^{-2}, while the projected area is (4-9) arcsec^2. This corresponds to a diameter of only 300 - 400 AU, assuming spherical simmetry. The compactness of this emission region will enable us to put constraints on the physical mechanisms responsible of the observed emission (see Sect. 4).

Using this emission area, the CO column density that we derive from the observed CO absolute line fluxes is N(CO) = $(0.7-2.0)10^{18}$ cm^{-2} and therefore an H_2O/CO abundance ratio

we assume a velocity linewidth dV, we can estimate both the column density and the emission region size.

The results of the model fitting are shown in Fig. 4 and Fig. 5 for ortho- and para-H_2O respectively. Almost all the lines in the LWS wavelength interval are well reproduced by the model. The differences in the flux level predicted in the two extreme models are quite small, indicating that the H_2O emission is not very sensitive to the exact value of temperature and density in

Fig. 6. Comparison of the modeled OH line fluxes (filled triangles) with those observed (open circles).

of ~ 0.1 - 0.7. Assuming a standard CO abundance of 10^{-4}, the water abundance with respect to H_2 is $\sim (1 - 7) \cdot 10^{-5}$. This value implies an enhancement with respect to the expected abundance in the ambient gas of at least a factor of 10 (e.g. Bergin et al. 1998).

High H_2O abundances are common in young stellar objects: the ISO spectrometers have in fact found strong emission from gas-phase H_2O from massive young stars (Harwit et al. 1998, González-Alfonso et al. 1998) and from low mass outflow driving sources (Liseau et al. 1996, Saraceno et al., in preparation, Ceccarelli et al. 1998) with abundances in the range $1-5 \cdot 10^{-5}$, rising to values as high as $\sim 5 \cdot 10^{-4}$ in L1448mm (Nisini et al. 1999b) and Orion (Harwit et al. 1998).

3.3. OH emission

For the OH models, we have considered 20 levels. The collisional downward rates are from Offer & van Dishoeck (1992) and the radiative decay rates are from the HITRAN catalogue (Rothman et al. 1987).

If we adopt the same parameters as derived from the above analysis also for the OH, we find that a better agreement between data and models is achieved with the lower temperature model (T = 300 K). The estimated OH column density is $N(OH) \sim 4 \cdot 10^{17}$ cm^{-2} and therefore a $X(OH) \sim 2.7 \cdot 10^{-5}$. The results of the OH model fitting are shown in Fig. 6. As can be seen from this figure, not all the lines can be reproduced by the models, in particular both the 163μm line and those shortward of 60μm.

Because T Tau is relatively bright in the continuum at the far infrared wavelengths (see Fig. 1), such a discrepancy could be due to the pumping from the local thermal radiation field. To test this possibility we also computed models for the OH

transitions including the field originated from dust at a temperature of 300K, using the model of Cesaroni & Wamsley (1991). We found that the inclusion of the local infrared radiation field increases the emission in the lines with λ less than 100μm and the 163μm line.

3.4. Atomic emission

The detection of [CII]158μm in the four off-source positions around T Tau (see Table 5) clearly shows that most of the ionized carbon emission ($\sim 80\%$) is from an extended region and not originated in the vicinity of T Tau. The intrinsic emission in the LWS beam centered on T Tau is about $2 \cdot 10^{-20}$ W cm^{-2}. This implies a ratio [OI]63μm/[CII]158μm of 115, greatly in excess of that expected from photodissociation region models (Kaufman et al.1999; Burton et al. 1990).

Finally the ratio of [OI]63μm/145μm=28.3 is such that no oxygen self-absorption should occur, as it often appears to be the case towards pre-main sequence sources (Saraceno et al. 1998). This suggests that there is no cold gas in front of the source, in accordance with the geometry of the outflow directed towards the observer.

As outlined in van den Ancker et al. (1999), based on a larger set of fine-structure lines detected at shorter wavelengths, we argue that the atomic line emission observed is consistent with the presence of J-type dissociative shocks. On the other hand, the excess [CII]158μm emission on-source could also be due to a local photodissociation region (PDR), possibly originated from the far-UV field of T Tau (see Sect. 4).
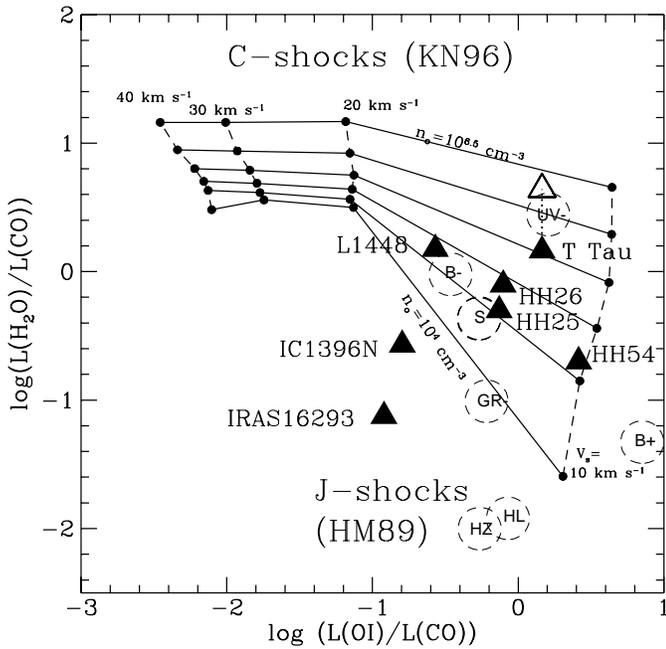
3.5. Total cooling

Table 6 summarises the physical quantities derived from the observed molecular spectra of CO, H_2O and OH, adopting the two models considered: the column densities and the total cooling luminosities are given for each molecular species. We also give the observed values of the cooling derived from the sum of all the detected fluxes. For deriving L_{H_2}, we used the line fluxes reported in van den Ancker et al. (1999) and the line H_2 1-0 S(1) at 2.12μm, given in Carr (1990). A comparison between the observed and modeled cooling shows that the observations of CO, H_2O and OH can account for most of the modeled cooling. The underestimate of the OH cooling by the 900 K model confirms that this latter is probably inadeguate to explain the observed OH emission. The total radiated cooling observed from these species, including [OI], sums up to about 0.04 $L_\odot$, and has to be considered as a lower limit. Taking the outflow parameters from the literature (Levreault 1988; Mundt 1984) we derive a total mechanical luminosity of about 0.05 $L_\odot$ (we have taken an average velocity of 10 km s^{-1}, a total outflow mass of 0.22 $M_\odot$, and a dynamical timescale of 40,000 years). The radiative luminosity observed in the far-infrared is therefore comparable to the outflow mechanical luminosity. This is expected if the stellar winds from the stars are driving the outflows and the shocks, traced by the far-infrared lines, accelerate the ambient medium into the molecular outflow (Davis & Eislöffel 1995).

Table 4. Measured OH line fluxes from the SWS (upper list) and LWS (lower list) grating spectrum, with 1σ uncertainties. Upper limits are at 3σ.

λ_{obs} (μm)	FWHM (μm)	Line id.	λ_{vac} (μm)	F (10^{-20} W cm^{-2})	ΔF
28.931	0.020	OH $^2\Pi_{1/2}7/2$-$^2\Pi_{3/2}5/2$	28.939	2.7	0.9
		OH $^2\Pi_{1/2}5/2$-$^2\Pi_{3/2}3/2$	34.603/34.629	<6.4	
43.950[†]	0.045[†]	OH $^2\Pi_{1/2}7/2$-$^2\Pi_{3/2}7/2$	43.950	5.2	1.5
53.17	0.75	OH $^2\Pi_{3/2}11/2$-$^2\Pi_{3/2}9/2$	52.93/53.06	61.2	4.4
		OH $^2\Pi_{1/2}3/2$-$^2\Pi_{1/2}3/2$	53.26/53.35		
55.91[†]	0.35	OH $^2\Pi_{1/2}9/2$-$^2\Pi_{1/2}7/2$	55.89/55.95	17.9	3.3
65.23	0.29	OH $^2\Pi_{3/2}9/2$-$^2\Pi_{3/2}7/2$	65.13/65.28	23.7	1.0
71.22	0.30	OH $^2\Pi_{1/2}7/2$-$^2\Pi_{1/2}5/2$	71.17/71.22	18.2	3.3
79.16[†]	0.29	OH $^2\Pi_{1/2}1/2$-$^2\Pi_{1/2}3/2$	79.12/79.18	17.8	3.0
84.59	0.59	OH $^2\Pi_{3/2}7/2$-$^2\Pi_{3/2}5/2$	84.42/84.60	25.9	2.4
98.73[†]	0.6	OH $^2\Pi_{1/2}5/2$-$^2\Pi_{1/2}3/2$	98.73	9.8	1.0
119.44		OH $^2\Pi_{3/2}5/2$-$^2\Pi_{3/2}3/2$	119.23/119.44	14.9	1.5
163.12[†]	0.6	OH $^2\Pi_{1/2}3/2$-$^2\Pi_{1/2}$-1/2	163.12/163.40	8.9	0.7

[†] wavelength was fixed for deblending.

Fig. 7. Total cooling from water lines versus [OI]63μm cooling, both normalized to the CO (high-J) cooling in few objects, including T Tau (filled triangles) and according to shock models. The open triangle shows the position that T Tau would have if the water cooling were increased by a factor 3. C-type shock models of Kaufman & Neufeld (1996) are shown in a grid where shock velocity increases from the right to the left from $10 < v_s < 40$ km s^{-1} (dashed lines) and density from the bottom to the top from 10^4 to $10^{6.5}$ cm^{-3} (solid lines). J-type shock models (Hollenbach & McKee 1989) are shown for comparison as large dashed circles, where S is the standard model, with preshock density of $n_o = 10^5$ cm^{-3}, shock velocity of $v_s = 80$ km s^{-1} and magnetic field of B $= 158\mu$G; UV-: the far-ultraviolet field is reduced by a factor of 10; B-: the magnetic field is reduced by a factor 10; B+: the magnetic field is increased by a factor 10; GR-: the grain size distribution is extended down to 10 Å; HL: H$_2$ formation on grains is equal to zero; HZ: H$_2$ formation heating is set to zero.

Table 5. Measured atomic line fluxes from the LWS grating spectrum with uncertainties.

Pos.	λ_{obs} (μm)	Line id.	λ_{vac} (μm)	F (10^{-20} W cm^{-2})	ΔF
on	63.21	[OI] $^3P_1 \rightarrow {}^3P_2$	63.18	230.6	1.0
on	145.52[†]	[OI] $^3P_0 \rightarrow {}^3P_1$	145.52	8.15	0.78
on	157.76	[CII] $^2P_{3/2} \rightarrow {}^2P_{1/2}$	157.74	10.6	0.5
off-N	157.80	[CII] $^2P_{3/2} \rightarrow {}^2P_{1/2}$	157.74	7.9	0.7
off-S	157.79	[CII] $^2P_{3/2} \rightarrow {}^2P_{1/2}$	157.74	8.8	1.2
off-W	157.76	[CII] $^2P_{3/2} \rightarrow {}^2P_{1/2}$	157.74	8.8	0.9
off-E	157.74	[CII] $^2P_{3/2} \rightarrow {}^2P_{1/2}$	157.74	9.1	0.7

[†] wavelength was fixed for deblending.

Table 6. Physical parameters of the molecular and atomic emission.

	observed[*]	"lower T"	"higher T"
Temperature T(K)		300	900
Density n_{H_2} (cm^{-3})		$4\cdot10^6$	$2\cdot10^5$
N_{CO} (cm^{-2})		$2 \cdot 10^{18}$	$7 \cdot 10^{17}$
N_{H_2O} (cm^{-2})		$2 \cdot 10^{17}$	$5 \cdot 10^{17}$
N_{OH} (cm^{-2})		$4\cdot10^{17}$	$4 \cdot 10^{17}$
L_{CO} (L$_\odot$)	0.0067	0.0096	0.010
L_{H_2O} (L$_\odot$)	0.008	0.014	0.009
L_{OH} (L$_\odot$)	0.012	0.019	0.009
$L_{[OI]}$ (L$_\odot$)	0.014	–	–
L_{H_2} (L$_\odot$)	0.005	–	–

[*] the observed cooling is computed by summing all the detected lines.

4. Discussion

Once the physical conditions of the emitting gas in the vicinity of T Tau have been established, we can now proceed to compare the results with existing models of shock excitation. The far-infrared line emission of young stellar objects is mainly originated from two physical processes: the excitation from photoionized and
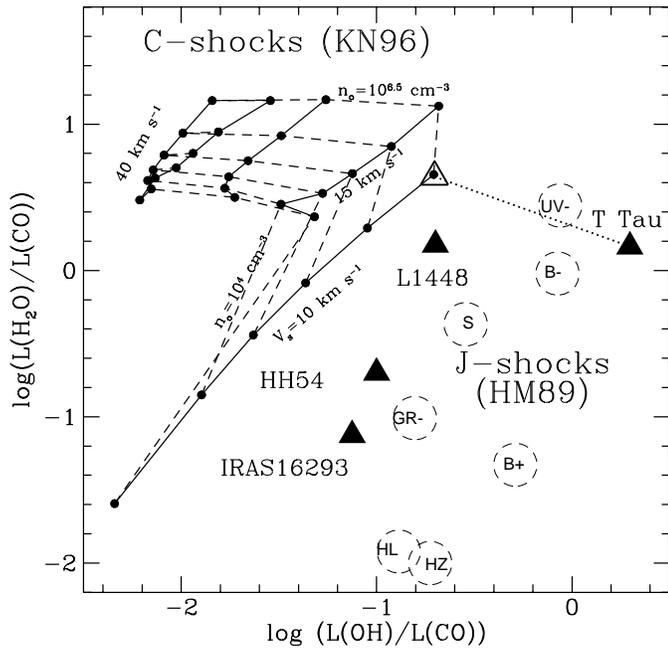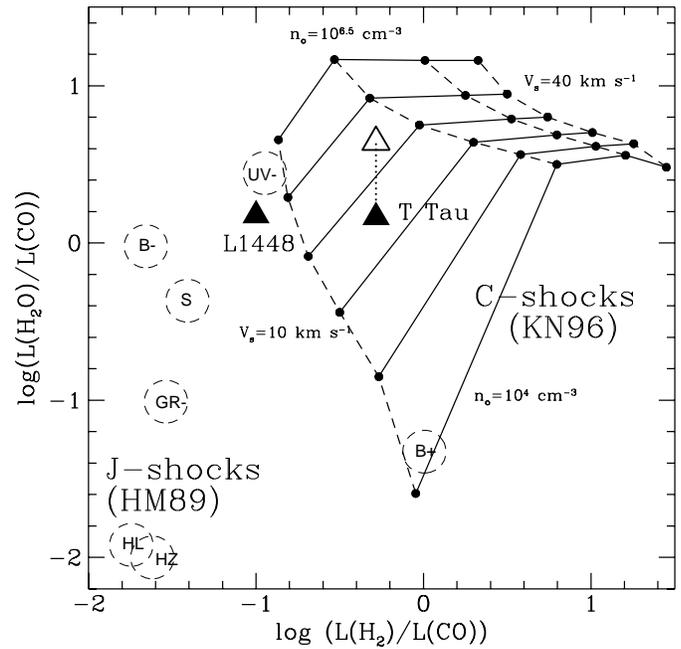
Fig. 8. Total cooling from water lines versus total cooling from OH lines, both normalized to the CO (high-J) cooling in few objects, including T Tau (filled triangles) and according to shock models. The open triangle shows the position that T Tau would have if the water cooling were increased by a factor 3 and the OH cooling decreased by a factor 10. C-type shock models of Kaufman & Neufeld (1996) are shown in a grid as a function of density and shock velocity. J-type shock models (Hollenbach & McKee 1989) are shown as large dashed circles (see caption of Fig. 7).

Fig. 9. Total cooling from water lines versus total cooling from H_2 lines, both normalized to the CO (high-J) cooling in T Tau and L1448 (Nisini et al. 1999b) (filled triangles) and according to shock models. The open triangle shows the position that T Tau would have if the water cooling were increased by a factor 3. C-type shock models of Kaufman & Neufeld (1996) are shown in a grid where density increases upward and shock velocity from the left to the right. J-type shock models (Hollenbach & McKee 1989) are shown as large dashed circles (see caption of Fig. 7).

photodissociated (PDR) regions (Tielens & Hollenbach 1985) and the shock excitation produced by the interaction of supersonic winds with the ambient medium. Depending on wind velocity, magnetic field and ion density, two kinds of shocks with different far-infrared spectra are predicted from models:

  i) high velocity dissociative J shocks (e.g. Hollenbach & McKee 1989), in which temperature, density and velocity have a discontinuous jump (J) on the shock front, molecules are dissociated and atomic lines are the dominant coolants;

 ii) low velocity non-dissociative C shocks (e.g. Kaufman & Neufeld 1996, Draine et al. 1983) in which the ion Alfvén velocity is larger than the shock velocity and the magnetic field transmits energy faster than the shock velocity; in this case temperature, density and velocity have a continuous (C) variation and molecules are the dominant coolants.

Instead of using intensities of many tens of different lines, we can obtain a better comparison between our data and the shock model predictions using the total cooling from a single species.

In Fig. 7 we show the water cooling as a function of the [OI]63μm cooling, both normalized to the high-J CO cooling. The C-type shock models of Kaufman & Neufeld (1996) are considered. The J-type shock models (Hollenbach & McKee 1989) are also indicated (see figure caption for details). To-

gether with the position of T Tau, we also show in this figure the positions of L1448 (Nisini et al. 1999b), IC1396 (Saraceno et al., in preparation), IRAS16293-2422 (Ceccarelli et al. 1998), and the Herbig-Haro objects HH54 (Liseau et al. 1996), HH25 and HH26 (Benedettini et al. 1999).

T Tau is in a central position, showing that both C-type and J-type shock models could explain the observations. It has to be noted, however, that according to Kaufman & Neufeld models, its position implies a shock velocity between 10 and 15 km s^{-1}, in a range where water production is triggered but it is not at its maximum efficiency. We can see in the figure that other pre-main sequence sources also cluster in the same region of T Tau, indicating that these shock conditions are fairly common in the environment of young stellar objects (Nisini et al. 1998).

Fig. 8 shows the water cooling as a function of the OH cooling, both normalized to the high-J CO cooling. As before, we consider both J-type and C-type shocks. The position of T Tau in this plot appears to be consistent with J-type shocks. The main reason why C-shocks fail to reproduce the observed cooling is the overabundance of OH molecules, by at least a factor 10. Only a model which includes the effects of the presence of a high UV field from T Tau itself can reproduce the observed values.

Fig. 9 shows the water cooling as a function of the H_2 cooling, both normalized to the high-J CO cooling. T Tau lies exactly

in the center of the region of C-type shocks and cannot be explained by J-type shocks. As expected, the strong H_2 emission cannot be accounted for by J-type shocks. We therefore rule out the hypothesis that the major responsible of the observed excitation are J-shocks.

Because photodissociation of water by an UV field, that is not included in shock models, can convert water to OH, we suppose that the overabundance of the OH molecule is due only to the strong far-UV radiation field associated to T Tau (Herbig & Goodrich, 1986). The photodissociation cross section of water at the $Ly\alpha$ frequency is in fact ten times larger than the one of OH (van Dishoeck & Dalgarno 1984). A similar situation has been found in supernova remnants, where OH 1720 MHz emission is explained as originated from C-type shocks, allowing that the action of an UV field creates sufficient OH from water dissociation (Wardle et al. 1999; Lockett et al. 1999).

If this is the case, the far-infrared molecular emission spectrum of T Tau is primarily due to C-type shocks. To reconcile the OH observations with C-type shock models we need that the OH abundance, and thus its total cooling, were reduced by a factor 10 in favor of water cooling. From Table 6, if we reduce by a factor 10 the OH column density and we increase of the corresponding amount that one of the water, passing from $2 \cdot 10^{17}$ to $5.6 \cdot 10^{17}$, we will increase the total water cooling by a factor of about 3.

Increasing the water cooling by this factor and decreasing the OH cooling by a factor 10 would move the position of T Tau in the three diagrams of Fig. 7, 8 and 9 in positions fully consistent with C-type shock models (see the open triangles in the figures), at pre-shock densities of about $10^{5.5-6}$ cm^{-3} and shock velocities of $10 < v_s < 20$ km s^{-1}. Comparing the pre-shock densities of these models with the densities derived from our LVG models, we found that a moderate compression factor (≤ 10) would be required. In support of the fact that the molecular emission is due to C-type shocks is the evidence of the presence of strong magnetic fields in the outflow region associated with T Tau S (Ray et al. 1997).

Our conclusion that the observed far-infrared molecular emission from T Tau can be explained by C-type shocks and that the atomic emission is probably originated in J-type shocks is in agreement with the findings of van den Ancker et al. (1999). Their models, based on the near to mid-infrared H_2 emission, imply two temperature components at 440 K and 1500 K, which again are roughly in agreement with our finding of two components: one ranging from 300 K to 900 K and another at an higher temperature traced by the higher J_{up} CO transitions.

As to the origin of the C-type shocks, responsible for the observed far-infrared molecular emission, we know from the LVG models that the emission region has a size of only few hundreds AU, assuming a spherical geometry. This implies that the shocks occur in a very compact region, presumably very close to the binary system. There are at least three mechanisms not mutually exclusive to explain the origin of the shocks:

1. from the interaction region of winds coming from the two stars;

2. from disk accretion on the youngest component of the binary system;
3. from the interaction of the stellar wind with the molecular material in the circumstellar envelope.

The first possibility seems the best one for originating fast ($v_s \sim 50$ km s^{-1}) dissociative J-type shocks, because the wind interaction would occur close to the stars where velocities are supposed to be high and the stellar field strong to dissociate molecules. The second possibility has already been suggested by Quirrenbach & Zinnecker (1997) to explain the near-infrared H_2 extended emission. The third one is probably at work in any case, because it is needed to explain the strong emission from CO, H_2O, OH, as well as that from H_2 (van den Ancker et al. 1999).

5. Conclusions

To summarise our results, we list the main findings of this study:

1. The far-infrared spectrum associated to the binary system of T Tau shows strong emission from CO, H_2O and OH molecules.
2. Optically thin CO emission lines from high-J transitions are used to constrain the physical regimes of the gas: T$\sim$300-900 K and $n_{H_2} \sim 10^{5-6}$cm^{-3}. The detection of CO lines with J_{up} of 24 and 25 seems to indicate that a warmer component is also needed.
3. H_2O and OH emission is consistent with such conditions, however the higher excitation lines at the shorter wavelenghs are not well fitted by these models, indicating that higher temperature gas should also be present, in agreement with the CO emission.
4. From the assumption that all the far-infrared molecular emission observed originate from the same region a very compact size of 300 - 400 AU of diameter is derived.
5. The detection of [CII]158μm off-source at large distances from T Tau shows that most of the ionised carbon emission ($\sim 80\%$) is from an extended region and not originated in the vicinity of T Tau. The intrinsic emission in the LWS beam centered on T Tau implies a ratio [OI]63μm/[CII]158μm of 115, much in excess of what is expected from photodissociation region models. This emission is probably due to J-type shocks, however it is not ruled out the possibility of a contamination by a PDR.
6. The total cooling observed in the various species is comparable to the mechanical luminosity of the outflow, indicating that the stellar winds could be the ultimate responsible of the line excitation through shocks.
7. The study of the cooling from the main radiative components ([OI], CO, H_2O, OH and H_2) is used to show that our data are consistent with C-type shock models, only if we assume an overabundance of the OH molecule (by a factor 10) probably due to the intense far-ultraviolet radiation field.
8. We finally consider the origin of the shocks responsible for the far-infrared emission: colliding winds from the components of the binary system, disk accretion in the more em-

bedded star and wind interaction with the molecular ambient cloud. Due to the large beam size of the LWS instrument, we are unable to specify which of the processes is the dominant one.

References

Adams F.C., Emerson J.P., Fuller G.A., 1990, ApJ 357, 606

Akeson R.L., Koerner D.W., Jensen E.L.N., 1998, ApJ 505, 358

Beckwith S.V.W., Gatley I., Matthews K., Neugebauer G., 1978, ApJ 223, L41

Beckwith S.V.W., Sargent A., Chini R. Guesten, R., 1990, AJ 99, 924

Benedettini M., Giannini T., Nisini B., et al., 1999, In: The Universe as seen by ISO, Cox P. & Kessler M.F. (eds.), ESA SP-427, Vol. 1, p. 471

Bergin E.A., Melnick G.J., Neufeld D.A., 1998 ApJ 499, 777

Böhm K.-H., Solf J., 1994, ApJ 430, 277

Burton M.G, Hollenbach D.J., Tielens A.G.G., 1990, ApJ 365, 620

Carr J.S., 1990, AJ 100, 1244

Ceccarelli C., Caux E., White G.J., et al., 1998, A&A 331, L17

Cesaroni R., Wamsley C.M., 1991, A&A 241, 537

Chackerian C., Tipping R.H., 1983, J. of Molecular Spectroscopy 99,431

Chandra S., Varshalovich D.A., Kegel W.H., 1984, A&AS 55, 51

Clegg P.E., Ade P.A.R., Armand C., et al., 1996, A&A 315, L38

Cohen M., Hollenbach D.J., Haas M.R., Erickson E.F., 1988, ApJ 329, 863

Davis C.J., Eislöffel J., 1995, A&A 300, 851

de Graauw T., Haser L.N., Beintema D.A., et al., 1996, A&A 315, L49

Draine B.T., Roberge W.G., Dalgarno A., 1983, ApJ 264, 485

Dyck H. M., Simon T., Zuckerman B., 1982, ApJ 255, 103

Edwards S., Snell R.L., 1982, ApJ 261, 151

Ghez A.M., Neugebauer G., Gorham P.W., et al., 1991, AJ 102, 2066

Giannini T., Lorenzetti D., Tommasi E., et al., 1999, A&A 346, 617

González-Alfonso E., Cernicharo J., van Dishoeck E., Wright C.M., Heras, A., 1998, ApJ 502, L169

Green S., Maluendes S., McLean A.D., 1993, ApJS 85,181

Harwit M., Neufeld D.A., Melnick G.J., Kaufman M.J., 1998, ApJ 497, L105

Herbig G.H., 1950, ApJ 111, 11

Herbig G.H., Goodrich R.W., 1986, ApJ 309, 294

Herbst T.M., Beckwith S.V.W., Glindemann A., et al., 1996, AJ 111, 2403

Herbst T.M., Robberto M., Beckwith S.V.W., 1997, AJ 114, 774

Hogerheijde M.R., van Langevelde H.J., Mundy L.G., Blake G.A., van Dishoeck E.F., 1997, ApJ 490, L99

Hogerheijde M.R., van Dishoeck E.V., Blake G.A., van Langevelde H.J. 1998, ApJ 502, 315

Hollenbach D., McKee C.F., 1989, ApJ 342,306

Kaufman M.J., Neufeld D.A., 1996, ApJ 456, 250

Kaufman M.J., Wolfire M.G., Hollenbach D.J., Luhman M.L., 1999, ApJ in press

Kessler M.F., Steinz J.A., Anderegg M.E., et al., 1996, A&A 315, L27

Kobayashi N., Nagata T., Hodapp K., Hora, J.L., 1994, PASJ 46, L183

Levreault R.M., 1988, ApJ 330, 897

Liseau R., Ceccarelli C., Larsson B., et al., 1996, A&A 315, L181

Lockett P., Gauthier E., Elitzur M., 1999, ApJ 511, 235

McKee C.F., Storey J.W.V., Watson D.M., Green S., 1982 ApJ 259, 647

Momose M., Ohashi N., Kawabe R. Hayashi M., Nakano T., 1996, ApJ 470, 1001

Mundt R., 1984, ApJ 280, 749

Nisini B., Giannini T., Molinari S., et al., 1998 in Star Formation with the Infrared Space Observatory, Yun J.L. & Liseau R. (eds.), ASP Conference Series, vol. 132, p.233

Nisini B., Benedettini M., Giannini T., et al., 1999a, A&A, 343, 266

Nisini B., Benedettini M., Giannini T., et al., 1999b, A&A 350,525

Offer A.R., van Dishoeck E.F., 1992, MNRAS 257, 377

Quirrenbach A., Zinnecker H., 1997, ESO Messenger 87, 36

Ray T.P., Muxlow T.W.B., Axon D.J., et al., 1997, Nat 385, 415

Reipurth B., Bally J., Levine D., 1997, AJ 114, 2708

Rothman L.S., Gamache R.R., Goldman A., et al., 1987, Appl.Opt., 26, 4078

Saraceno P., Nisini B., Benedettini M., et al., 1998, in Star Formation with the Infrared Space Observatory, Yun J.L., Liseau R. (eds.), ASP Conference Series, vol. 132, p.233

Schuster K.-F., Harris A.I., Anderson N.L., Russell A.P.G., 1993, ApJ 412, L67

Schuster K.-F., Harris A.I., Russell A.P.G., 1997, A&A 321, 568

Stapelfeldt K.R., Burrows C.J., Krist J.E., et al., 1998, ApJ 508, 736

Swinyard B.M., Burgdorf M.J., Clegg P.E., et al., 1998, Proc. SPIE, Vol.3354, p.888, Infrared Astronomical Instrumentation, Albert M. Fowler (ed.), 1998.

Tielens A.G.G.M., Hollenbach D., 1985, ApJ 291, 722

van den Ancker M.E., Wesselius P.R., Tielens A.G.G.M., van Dishoeck E.F., Spinoglio L., 1999, A&A 348, 877

van Dishoeck E.F., Dalgarno A., 1984, Icarus 59, 305

Wardle M., Yusef-Zadeh F., Geballe T.R., 1999, In: The Central Parsecs of the Galaxy, Falke H., Cotera A., Duschl W.J., Melia F., Rieke M.J. (eds.), ASP Conference Series, Vol. 186, p. 432

Weintraub D.A., Zuckerman B., Masson C.R., 1989, ApJ 344, 915

Wichmann R., Bastian U., Krautter J., Jankovics I., Rucinski S. M., 1998, MNRAS 301, L39